High-Speed Compact Plasmonic-PdSe$_2$ Waveguide-Integrated Photodetector

Jialing Jian,[#] Jianghong Wu,[#] Chuyu Zhong, Hui Ma, Boshu Sun, Yuting Ye, Ye Luo, Maoliang Wei, Kunhao Lei, Ruizhe Liu, Zequn Chen, Guangyi Li, Hao Dai, Renjie Tang, Chunlei Sun, Junying Li, Wei Li, Ming Li,* Hongtao Lin,* and Lan Li*

Read Online

ACCESS | Metrics & More | Article Recommendations | Supporting Information

ABSTRACT: Waveguide-integrated photodetectors are essential components in integrated photonic circuits since they facilitate light conversion into electrical signals. Nonetheless, optical absorption and carrier collection can significantly affect the device performance. As a solution to this issue, plasmonic slot waveguides confine optical energy within a subwavelength scale in a photoconductive detector, enhancing optical absorption and providing extremely short channels to collect carriers. Two-dimensional van der Waals layered palladium selenide (PdSe$_2$) exhibits the merits of a narrow bandgap and high carrier mobility, thus positioning it as a favorable candidate material for photodetectors operating at the telecommunication band. In this study, we propose and experimentally verify a high-speed PdSe$_2$-plasmonic waveguide-integrated photodetector with a dark current of 4.5 μA and an intrinsic responsivity of 560.1 mA·W^{-1} at 3 V. Additionally, it has an internal quantum efficiency of 32.3%, and the measured 3 dB bandwidth is 17.5 GHz. This integrated photodetector fulfills the requirements of various critical applications in optical communication, microwave photonics, sensing, and imaging.

KEYWORDS: integrated photodetector, plasmonics, slot waveguide, PdSe$_2$
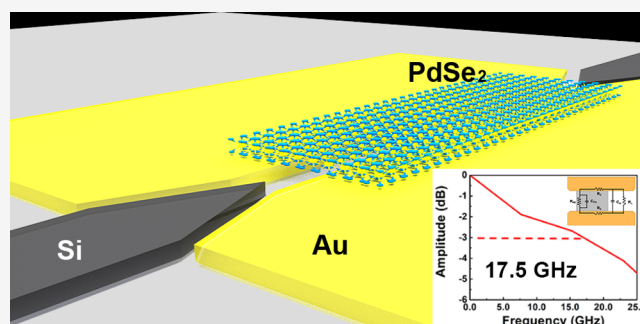
INTRODUCTION

Modern communication systems require the hybrid integration of electronic and photonic systems to meet the demands of ever-increasing data rates (Tb·s^{-1} data rates) in data centers, wireless communications, and computing infrastructures.[1−3] Integrated photonic devices based on plasmonic structures offer numerous benefits for the next generation of communication, nonlinear photonics and sensitive sensing systems.[4−6] Plasmonic structures provide deep-subwavelength confinement of the light field, which enhances optical confinement and light−matter interactions, significantly influencing the device performance efficiency and speed. Ultrafast, efficient, and compact electro-optic plasmonic modulators have already achieved bandwidths exceeding 500 GHz.[7−9] However, there is still a need to further explore plasmonic-structure-based photodetectors with both high speed and responsivity.

Plasmonic-based integrated photonic circuits require photodetectors that integrate photoactive materials with plasmonic waveguides.[10−12] However, integrating materials such as germanium films with waveguide-integrated photodetectors presents challenges due to threading dislocations and surface roughness at the interface, resulting from lattice mismatch.[13] Germanium also faces limitations in the mid-infrared band due to its inappropriate optical bandgap.[10] Colloidal quantum dots, while able to operate in the mid-infrared band, have limited response speeds because of their carrier mobility.[14] A promising alternative is van der Waals materials (VDWMs), which are bound by weak van der Waals forces and allow for their transfer on various substrates, making them a compelling option to mitigate the challenges of integrating different material platforms caused by variations in thermal expansion coefficients and lattice parameters. VDWMs are an emerging photoactive material with significant potential for use in plasmonic-based integrated photonic circuits.[14−16] Graphene is ideally suited for use as a waveguide-integrated photodetector in the telecommunication and mid-infrared regions (MIR) because of its high mobility and wide optical absorption range.[17−20] However, graphene photodetectors suffer from large dark currents and shot noise due to their zero band gap.[21]

Black phosphorus photodetectors have high responsivity[22,23] but require protection from degradation caused by exposure to water or oxygen.[24] PdSe$_2$ is air-stable and exhibits a high carrier mobility. Several advanced material fabrication methodologies have been developed to grow high-quality PdSe$_2$ thin films for the scalable production of PdSe$_2$-based devices.[25,26] The band gap of PdSe$_2$ spans from 1.2 eV in monolayer to 0.03 eV in bulk material, which brings about effective optical absorption at the MIR region.[27−29]

In relevant reports, waveguide photodetectors based on PdSe$_2$ are limited in bandwidth due to excessively long channels, and the weak optical absorption leads to low responsivity.[30,31] To address this problem, plasmonic slot waveguides are used to provide short drift paths for photogenerated carriers and fast photoresponses. Besides, a plasmonic slot waveguide usually provides subwavelength mode confinement, thus enhancing light−matter interaction.[12,18,32] The plasmonic-PdSe$_2$ waveguide-integrated photodetectors have a high responsivity and internal quantum efficiency (IQE) with a high-speed photoresponse due to the plasmonic design concept. Moreover, the proposed device operates over a broad spectral range, making it suitable for efficient photodetection at high speed.[14] As a result, the present plasmonic-PdSe$_2$ waveguide-integrated photodetectors possess an intrinsic (extrinsic) responsivity as high as 560.1 (236.9) mA·W^{-1} and an IQE of 32.3% at a wavelength of 1550 nm. The 10 μm-long device possesses a low noise equivalent power (NEP) of 17.9 pW·Hz$^{-0.5}$ and a fast photoresponse rate of 17.5 GHz.

RESULTS

The proposed photodetector is shown in Figure 1a, comprising three primary components: a pair of grating couplers and
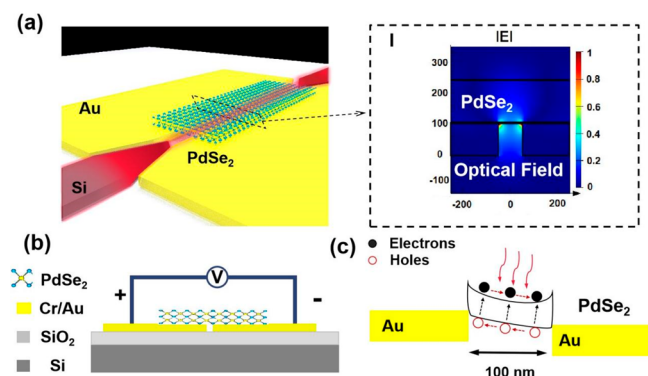

Figure 1. Conceptual illustration of the photodetector design. (a) 3D schematic representation of the plasmonic-PdSe$_2$ waveguide photodetector. Light is introduced into the plasmonic-PdSe$_2$ photodetector through a silicon waveguide via evanescent coupling. The inset (I) shows the optical field distribution for the PdSe$_2$-plasmonic slot waveguide photodetector (slot width: 100 nm, waveguide height: 100 nm, PdSe$_2$ layer thickness: 142 nm). (b) Cross-sectional view of the proposed photodetector. (c) Energy band diagram of the proposed photodetector junction under illumination at a bias voltage.

silicon-to-SPP mode converters and a plasmonic slot waveguide featuring a PdSe$_2$ thin film atop it. The plasmonic slot waveguide comprises two metallic films whose interfaces support a surface plasmon polaritons (SPPs) mode. The plasmonic slot waveguide improves the optical confinement in the nanoscale active core compared with a Si-wire waveguide.

At the same time, the SPP's transverse electric (TE) mode in the plasmonic slot waveguide is parallel to the interface of PdSe$_2$, which promotes PdSe$_2$-light interaction. The optical energy is absorbed while propagating in the area covered by 142 nm-thick PdSe$_2$ (inset I of Figure 1a). We have explained the reasons for choosing a thicker PdSe$_2$ in the Supporting Information, S1. We simulated the optical field distribution of a device with two different thicknesses of PdSe$_2$ (Supporting Information, Figure S1). Figure 1b presents a cross-sectional view of the proposed plasmonic-PdSe$_2$ waveguide-integrated photodetector with a slot waveguide width of 100 nm, designed to offer exceedingly narrow drift paths for the carriers of PdSe$_2$. Meanwhile, Figure 1c visually demonstrates the device's band diagram under bias voltage conditions. The Au has a higher work function than PdSe$_2$, resulting in an upward energy band bending, which hinders carrier transport and results in minimal dark current.

The scanning electron microscopy (SEM) image shows the two different parts of the devices in Figure 2a. The slot waveguide has a length of 10 μm. These structures transform the photonic mode of the photonic waveguide, with the dimension of typically $w_{Si} \times h_{Si}$ (450 nm × 220 nm), into the plasmonic slot waveguide with the size of approximately $w_{slot} \times h_{slot}$ (100 nm × 100 nm). The influence of gold film roughness inhomogeneity and fabrication alignment on propagation loss is within the acceptable tolerance, as demonstrated in Figure 2a, inset I. The optical microscope image of the fabricated sample is illustrated in inset II of Figure 2a. The thickness of PdSe$_2$ was measured to be 142 nm by Atom Force Microscopy (AFM), as indicated in Figure 2b. To confirm the quality of the PdSe$_2$ film, we conducted Raman spectroscopy of the multilayer PdSe$_2$ after the fabrication process. The obtained findings are in line with prior research, where A$_g$ peaks were situated at 143, 206, and 264 cm^{-1} and the B$_{1g}$ mode was detected at 229 cm^{-1}, as shown in Figure 2c. Notably, no additional discernible Raman peaks were observed, affirming the absence of defects introduced during the fabrication process. Figure 2d shows an output optical power change of a 10 μm-long plasmonic slot waveguide after transferring a PdSe$_2$ flake (length: 9.46 μm; thickness: 142 nm) upon it. The PdSe$_2$ flake's absorption coefficient (α_m) at 1550 nm is determined to be 0.81 dB/μm, calculated from the discrepancy in optical power measured before and after transferring the device.

Figure 3 illustrates the optoelectronic characteristics of a plasmonic-PdSe$_2$ waveguide photodetector (S1, with a 9.46 μm-long and 142 nm-thick PdSe$_2$ patch). An evaluation of these characteristics was conducted with the aid of a probe station that featured fiber-coupling capabilities. Figure 3a demonstrates the IV curves of sample S1, both in the absence of illumination (dark) and under 1550 nm illumination. The linear nature of the IV curve in the dark verified that the contact between PdSe$_2$ and the electrode is ohmic. Additionally, there is no observed photocurrent at 0 V, which excludes the photovoltaic and photothermoelectric effects. The possibility of the bolometric effect is eliminated as the photocurrent exhibits a nonlinear increase with the applied bias voltage.[33] Therefore, the dominant mechanism for photocurrent generation in this type of photodetectors is the photoconductive effect. The applied external electric field leads to the separation and accumulation of electron−hole pairs, inducing a photocurrent with a positive correlation to the optical signal intensity, as the photogenerated carriers migrate toward the metal electrode. The dark current increasing with
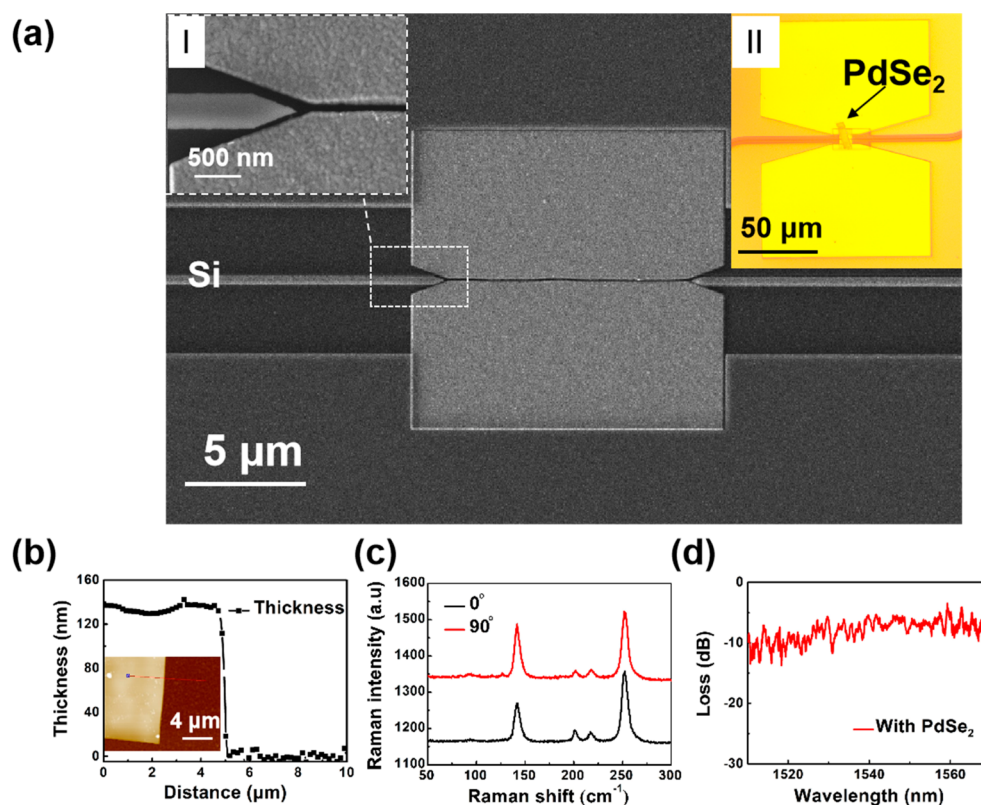
Figure 2. Diagram of photodetector preparation and characterization. (a) SEM image of the 10 μm-long plasmonic slot waveguide. The photograph is taken before transferring the PdSe$_2$ layer. The top inset (I) shows the alignment details of the waveguide taper to the plasmonic mode converter. (II) Optical image of a plasmonic-PdSe$_2$ slot waveguide integrated photodetector. (b) PdSe$_2$ film thickness measured by AFM. The optical image of the proposed sample is depicted in the inset. (c) Raman spectra of a multilayer PdSe$_2$ measured at a wavelength of 532 nm for two different polarization states. (d) Optical loss of the plasmonic slot waveguides after transferring a PdSe$_2$ flake (length: 9.46 μm, thickness: 142 nm).

the thicker thickness is 4.5 μA at 3 V. The dark current (blue line) is significantly less than that of metal−graphene−metal photoconductors.[32,34] Several samples have been prepared and characterized for comparison with the summarized results presented in Table S1.

Figure 3b shows the measured increasing photocurrent with increasing optical power levels at 3 V. The photodetector's responsivity (R) is characterized as $R = I_{ph}/P_{in}$, where I_{ph} and P_{in} denote the photocurrent and input optical power (Supporting Information, part S2). The R decreases from 236.9 mA W^{-1} to 10.6 mA W^{-1} as the input power escalates from 1 to 100 μW (Figure 3b, red line) at 3 V. Such an external responsivity surpasses that of counterparts utilizing graphene,[17] MoSe$_2$,[35] and PtSe$_2$.[36]

Figure 3c shows the bias voltage-dependent responsiveness of the proposed devices, which suggests that a higher bias voltage will result in a higher photoinduced carrier generation-separation efficiency. Plasmonic slot waveguides can enhance the light−PdSe$_2$ interaction, but they also generate an internal optical loss that restricts light absorption and photocarrier generation, resulting in limitations in the detector's overall responsivity and quantum efficiency. Therefore, it is crucial to consider the optical loss of a plasmonic waveguide for calculating the detector's intrinsic responsivity (R_{int}), defined as $R_{int} = I_{ph}/P_{photo\_int}$. Here, P_{photo_int} is the optical energy absorbed by a PdSe$_2$ flake, which is defined as the $P_{photo\_int} = \eta_m * P_{in}$.[22,37,38] In this scenario, the effective light absorption ratio (η_m) is calculated to be ~42.4% (Supporting Information,

part S2), and R_{int} is estimated to be 463.9 mA·W^{-1} at the input power of 1.2 μW. With the increasing input optical powers from 1 to 100 μW, the value of R_{int} diminishes from 560.1 mA·W^{-1} to 25.2 mA·W^{-1}. The elevated intrinsic responsivity aligns with a high IQE, which is determined from IQE = $R_{int} \times \hbar\omega/q$. Here, $\hbar$, ω, and q are the reduced Planck constant, the light angular frequency, and the elementary charge.[37] Figure 3c depicts the variation of IQE at different voltages, which can reach as high as 32.3% (represented by the red dots on the right y-axis).

As shown in Figure 3d, the photodetector exhibits a broad spectral photoresponse characteristic, with a responsivity exceeding 143.5 mA·W^{-1} within this range at an input optical power of 1.2 μW and a voltage of 3 V. The observed fluctuating responsivity can be attributed to variations in incident power at different wavelengths due to variations in the coupling efficiencies of the grating couplers. Despite this, a flat response was observed across almost the entire optical communications C-band (1530−1565 nm). Moreover, previous works have reported that plasmonic-PdSe$_2$ photo-detectors can operate at wavelengths in the MIR range.[31]

When assessing the noise characteristics of a photodetector, it is typically necessary to consider $1/f$ noise in the low-frequency region, Johnson noise, and dark current shot noise. The plasmonic-PdSe$_2$ photodetectors exhibit typical $1/f$ noise characteristics, as illustrated in Figure 4a. The measured $1/f$ noise diminishes from 1.7×10^{-20} A^2·Hz^{-1} at 1 Hz to 4.3×10^{-25} A^2·Hz^{-1} at 100 kHz at 3.0 V. These characteristics can be
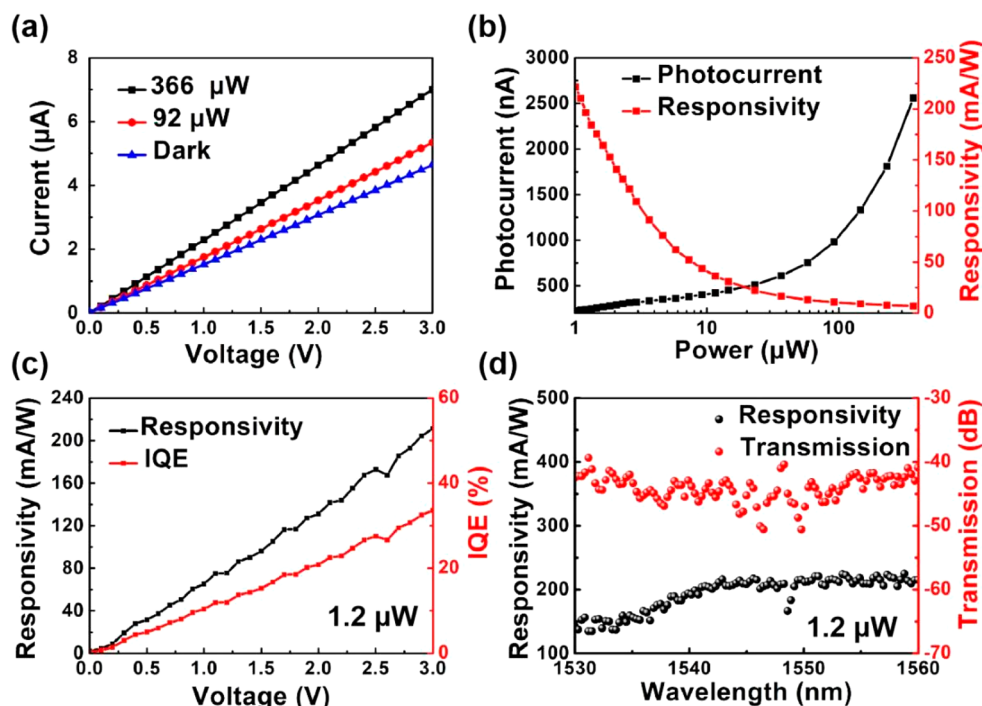
Figure 3. Optoelectronic characteristics of plasmonic-PdSe$_2$ photodetector (S1, with 9.46 μm-long, 142 nm-thick PdSe$_2$ thin film). (a) Current–voltage (IV) characteristics of a plasmonic-PdSe$_2$ waveguide-integrated photodetector under both dark and illuminated conditions at varying optical power levels at 1550 nm. (b) Photocurrent (black line) and responsivity (red line) versus incident optical power at 3 V. (c) Responsivity (left axis) and IQE (right axis) under applied voltages ranging from 0 to 3 V at the input optical power of 1.2 μW. (d) Spectral response of plasmonic-PdSe$_2$ photodetectors at an input optical power of 1.2 μW.
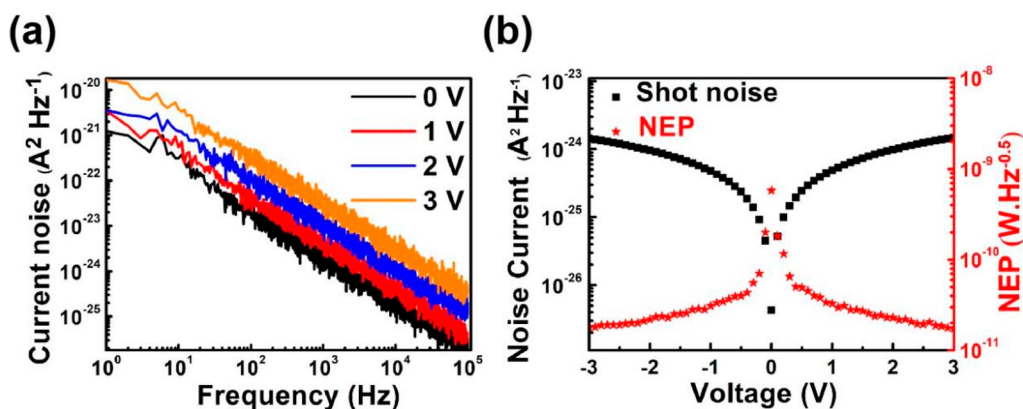

Figure 4. Noise characteristics of plasmonic-PdSe$_2$ photodetector (S1, with 9.46 μm-long, 142 nm-thick PdSe$_2$ thin film). (a) Spectral analysis of 1/f noise in the proposed photodetector (S1) at varying applied voltages. (b) NEP and shot noise arising from the noise current at varying bias voltages.

quantified using Hooge's empirical relationship,[39,40] while a higher external bias voltage enhances responsivity but also triggers an increase in 1/f noise. The shot noise can be represented as $S_s = 2qI_d\Delta f$, where I_d and Δf denote the dark current and bandwidth. The calculated shot noise of sample S1 is 1.5×10^{-24} A^2·Hz^{-1}, which corresponds to a dark current of 4.5 μA at 3.0 V. The thermal noise (associated with Johnson noise) is estimated to be 2.5×10^{-26} A^2·Hz^{-1} at 3.0 V according to $S_t = 4kT\Delta f/R_s$, where k, T, and R_s are the Boltzmann constant, the temperature (300 K, sample S1), and the resistance of the device, respectively.[41] The NEP serves as the most suitable figure of merit for waveguide-integrated photodetectors, quantifying the detector's signal-to-noise ratio performance. Constrained primarily by dark-current shot noise,

our analysis shows that the photodetector achieves a room-temperature NEP of 17.9 pW·Hz$^{-0.5}$. Moreover, the current noise for a plasmonic-PdSe$_2$ photodetector increase as the applied voltage increases, whereas the NEP demonstrates an inverse dependence on voltage in Figure 4b. Attributed to the application of a higher bias voltage, this phenomenon is marked by an increased efficiency in the separation and collection of photogenerated carriers, coupled with a higher responsivity.

The photodetector's frequency response was estimated through impulse response testing, with the setup depicted in Figure 5a. The optical pulse generated by a mode-locked laser with a 150 fs duration and a central wavelength of 1560 nm is coupled into the photodetector. Subsequently, a sampling
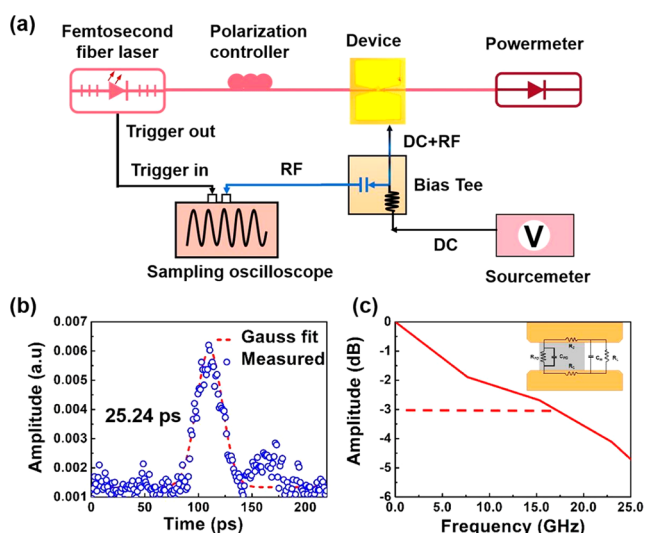
(a)

(b) **(c)**

Figure 5. Frequency response of the proposed photodetector (S1). (a) Setup for experimental measurement of the impulse response. (b) Impulse response of the proposed photodetector (sample S1). (c) Fourier Transform representation of the time-domain pulse signal generated by device S1. The inset illustrates the equivalent high-frequency circuit of the device.

oscilloscope with a detection bandwidth of 60 GHz was employed to capture the output electrical pulse signals of the proposed photodetector. As the light traveled through several meters of fiber, an attenuator, and a sampling oscilloscope, the optical pulse width increased to approximately 6.15 ps before reaching the photodetector due to a dispersion effect (Supporting Information, S3). The full width at half maximum of the electrical pulse is denoted as Δt for sample S1 and is about 25.2 ps, as illustrated in Figure 5b. The 3 dB bandwidth (Δf), calculated using the time-bandwidth product formula ($\Delta f \cdot \Delta t = 0.441$), was determined to be 17.5 GHz.[42,43] The frequency response of the device, derived from the Fourier transform of the time-domain data, is presented in Figure 5c. Typically, the bandwidth of a photodetector can be influenced by two factors: the carrier transit time (τ_{tr}) and the resistance-capacitance (RC) time (τ_{RC}) constant.[44] The bandwidth constrained by carrier transit time can be calculated using the formula $f_t = 1/(2\pi\tau_{tr})$, where τ_{tr} represents the carrier transit time within the detector channel. The τ_{tr} can be computed by $\tau_{tr} = L^2/(2\mu V_{bias})$, where L denotes the detector channel (the slot width), μ represents the mobility of PdSe$_2$ flake, and the V_{bias} was set at 3 V. The mobility of PdSe$_2$ flake (~24.0 nm, 40 layers)[45] was taken as 28.1 cm$^2\cdot$V$^{-1}\cdot$s^{-1} based on the ref 45. The calculated τ_{tr} is about 0.59 ps at 3 V. Subsequently, the calculated bandwidth determined by the carrier transit time amounts to ~267 GHz. In our experiment, the observed frequency responses remained nearly consistent across various thicknesses and bias voltages. This suggests that carrier mobility is not the primary limiting factor affecting the response speed of the photodetectors in this study.

We utilized the high-frequency equivalent circuit, as shown in Figure S4a to calculate the RC time constant, subsequently determining the bandwidth constrained by the RC coefficients. Initially, the high-frequency impedance Z_{in} can be computed based on the formula $Z_{in} = Z_o*((1 + S_{11})/(1 - S_{11}))$, where Z_o represents the system impedance (50 Ω).[44,46] The reflection coefficient S_{11} of the photodetector was then measured by using a vector network analyzer (VNA). The total resistance R_c

of sample S1 was calculated to be 34.5 Ω for the 10 μm length of the PdSe$_2$ thin film (Supporting Information, Figure S4b). We derived the total capacitance (C_{PD}) by considering two components: the capacitance of the metal contacts (C_m) in the RC equivalent model and the capacitance of the 2D material (C_{PdSe2}). According to measurement, the C_{PD} of the device was calculated to be 83.6 fF, as shown in Figure S4b of the Supporting Information. The RC-time limited bandwidth is $1/(2\pi R_{total} C_{PD}) = 22.5$ GHz. According to the formula $f_{RC} = 1/(2\pi \cdot R_{total} C_{PD})$ ($R_{total} = R_e + R_L$, $R_L = 50$ Ω), the bandwidth constrained by the RC constant is calculated to be 22.5 GHz. The value of f_{RC} closely approximates the measured bandwidth, in contrast to the carrier-limited bandwidth. This suggests that the primary limiting factor for the bandwidth of our presented photodetector is attributed to RC parameters of the device.

The speed response of the device is improved by adding gates to the upper layers of the device so that the upper carriers can be separated and transmitted faster.[18,47] To further enhance the plasmonic field localization characteristics, preparing a slot waveguide on top of PdSe$_2$ should be considered as an optimization method for device fabrication.[17] Furthermore, the considerable optical losses of the grating coupler and photonic to plasmonic mode conversion led to an optical power budget issue, ultimately limiting the amplitude of the converted electrical signal. Ideally, an optimal solution would entail the utilization of a trans-impedance amplifier to effectively amplify the RF signal, thus enhancing overall performance.[12]

◼ CONCLUSION

Waveguide-photodetectors have demonstrated promise in the realization of active silicon photonic circuits operating at infrared wavelengths. However, current technologies are limited by the trade-off between responsivity and fundamental bandwidth constraints. Here, we design and experimentally fabricate a plasmonic-PdSe$_2$ waveguide-integrated photo-detector with a measured bandwidth beyond 17 GHz, covering C-band (1530−1565 nm) telecom wavelength. Simultaneously, an intrinsic (extrinsic) responsivity up to 560.1 (236.9) mA·W^{-1} is obtained with static measurements revealing an IQE of up to 32.3%. Additionally, this photodetector shows an NEP of 17.9 pW·Hz$^{-0.5}$. The PdSe$_2$-plasmonic-based wave-guide photodetector provides a route for high-performance integrated photodetector utilizing various critical applications in optical communication, microwave photonics, sensing, and imaging.

◼ EXPERIMENTAL METHODS

Device Fabrication. Optical devices were manufactured on a commercially available silicon-on-insulator substrate, featuring a top silicon layer measuring 220 nm in thickness and a 3 μm-thick buried oxide layer. Grating couplers and waveguides were patterned using electron beam lithography (EBL) with a Raith Voyager system, followed by dry etching using Samco RIE-101iPH equipment. The dimensions of the Si waveguide are defined as width × height = 450 nm × 220 nm. Subsequently, the plasmonic slot waveguide was fabricated through EBL patterning, followed by e-beam evaporation of Au, and subsequently, it was achieved via a lift-off process. In the end, the multilayer PdSe$_2$ flakes were exfoliated from bulk PdSe$_2$ crystal (Taizhou SUNANO New Energy CO., Ltd.) by

Scotch tape. These flakes were meticulously positioned and transferred onto the prefabricated devices with the help of polydimethylsiloxane, all done under a microscope.

Measurement. The light source used for static optoelectronic testing of the device is a tunable semiconductor laser with a wavelength range adjustable between 1260 and 1620 nm (Santec Corporation, TSL-550), while electrical testing is accomplished through a semiconductor analyzer (PDA, FS-Pro). An optical pulse outputted from the erbium fiber laser (NPI Rainbow 1550 OEM) was coupled to the photodetector. The sampling oscilloscope (60 GHz bandwidth, Agilent DSO9404A) collected the output electrical pulse signal of the device. The photodetector was powered by a source meter (Keithley 2450). The resulting AC photocurrent was subsequently isolated using a bias-tee (Anritsu, G3N46, Bandwidth: 8 kHz-60 GHz). The photocurrent signal was retrieved via a microwave probe and then reintroduced into the input port of the parameter network analyzer. The S_{11} parameter could be obtained from the VNA (Anritsu MS4647B) measurement for the total impedance.

■ ASSOCIATED CONTENT

ⓢ Supporting Information

The Supporting Information is available free of charge at https://pubs.acs.org/doi/10.1021/acsphotonics.3c00453.

S1: Simulation for optical absorption of the PdSe$_2$ film. S2: Calculation of intrinsic responsivity and internal quantum efficiency. S3: Measurement of the ultrafast photoresponse. S4: Measurement and calculation RC of the plasmonic-PdSe$_2$ photodetector (PDF)

■ AUTHOR INFORMATION

Corresponding Authors

Lan Li − *Key Laboratory of 3D Micro/Nano Fabrication and Characterization of Zhejiang Province, School of Engineering, Westlake University, Hangzhou 310030, China; Institute of Advanced Technology, Westlake Institute for Advanced Study, Hangzhou 310024, China;* ⓞ orcid.org/0000-0002-9097-9157; Email: lilan@westlake.edu.cn

Hongtao Lin − *State Key Laboratory of Modern Optical Instrumentation, Key Laboratory of Micro-Nano Electronics and Smart System of Zhejiang Province, College of Information Science and Electronic Engineering, Zhejiang University, Hangzhou 310027, China;* ⓞ orcid.org/0000-0001-7432-3644; Email: hometown@zju.edu.cn

Ming Li − *State Key Laboratory on Integrated Optoelectronics, Institute of Semiconductors, Chinese Academy of Sciences, Beijing 100083, China;* Email: ml@semi.ac.cn

Authors

Jialing Jian − *Zhejiang University, Hangzhou 310027, China; Key Laboratory of 3D Micro/Nano Fabrication and Characterization of Zhejiang Province, School of Engineering, Westlake University, Hangzhou 310030, China; Institute of Advanced Technology, Westlake Institute for Advanced Study, Hangzhou 310024, China;* ⓞ orcid.org/0000-0001-6809-6588

Jianghong Wu − *Key Laboratory of 3D Micro/Nano Fabrication and Characterization of Zhejiang Province, School of Engineering, Westlake University, Hangzhou 310030, China; Institute of Advanced Technology, Westlake Institute for Advanced Study, Hangzhou 310024, China*

Chuyu Zhong − *State Key Laboratory of Modern Optical Instrumentation, Key Laboratory of Micro-Nano Electronics and Smart System of Zhejiang Province, College of Information Science and Electronic Engineering, Zhejiang University, Hangzhou 310027, China*

Hui Ma − *State Key Laboratory of Modern Optical Instrumentation, Key Laboratory of Micro-Nano Electronics and Smart System of Zhejiang Province, College of Information Science and Electronic Engineering, Zhejiang University, Hangzhou 310027, China*

Boshu Sun − *Key Laboratory of 3D Micro/Nano Fabrication and Characterization of Zhejiang Province, School of Engineering, Westlake University, Hangzhou 310030, China; Institute of Advanced Technology, Westlake Institute for Advanced Study, Hangzhou 310024, China*

Yuting Ye − *Key Laboratory of 3D Micro/Nano Fabrication and Characterization of Zhejiang Province, School of Engineering, Westlake University, Hangzhou 310030, China; Institute of Advanced Technology, Westlake Institute for Advanced Study, Hangzhou 310024, China*

Ye Luo − *Key Laboratory of 3D Micro/Nano Fabrication and Characterization of Zhejiang Province, School of Engineering, Westlake University, Hangzhou 310030, China; Institute of Advanced Technology, Westlake Institute for Advanced Study, Hangzhou 310024, China*

Maoliang Wei − *State Key Laboratory of Modern Optical Instrumentation, Key Laboratory of Micro-Nano Electronics and Smart System of Zhejiang Province, College of Information Science and Electronic Engineering, Zhejiang University, Hangzhou 310027, China*

Kunhao Lei − *State Key Laboratory of Modern Optical Instrumentation, Key Laboratory of Micro-Nano Electronics and Smart System of Zhejiang Province, College of Information Science and Electronic Engineering, Zhejiang University, Hangzhou 310027, China*

Ruizhe Liu − *State Key Laboratory of Modern Optical Instrumentation, Key Laboratory of Micro-Nano Electronics and Smart System of Zhejiang Province, College of Information Science and Electronic Engineering, Zhejiang University, Hangzhou 310027, China*

Zequn Chen − *Key Laboratory of 3D Micro/Nano Fabrication and Characterization of Zhejiang Province, School of Engineering, Westlake University, Hangzhou 310030, China; Institute of Advanced Technology, Westlake Institute for Advanced Study, Hangzhou 310024, China*

Guangyi Li − *State Key Laboratory on Integrated Optoelectronics, Institute of Semiconductors, Chinese Academy of Sciences, Beijing 100083, China*

Hao Dai − *State Key Laboratory of Modern Optical Instrumentation, Key Laboratory of Micro-Nano Electronics and Smart System of Zhejiang Province, College of Information Science and Electronic Engineering, Zhejiang University, Hangzhou 310027, China*

Renjie Tang − *Key Laboratory of 3D Micro/Nano Fabrication and Characterization of Zhejiang Province, School of Engineering, Westlake University, Hangzhou 310030, China; Institute of Advanced Technology, Westlake Institute for Advanced Study, Hangzhou 310024, China*

Chunlei Sun − *Key Laboratory of 3D Micro/Nano Fabrication and Characterization of Zhejiang Province, School of Engineering, Westlake University, Hangzhou 310030, China; Institute of Advanced Technology, Westlake Institute for Advanced Study, Hangzhou 310024, China*

Junying Li − *State Key Laboratory of Modern Optical Instrumentation, Key Laboratory of Micro-Nano Electronics and Smart System of Zhejiang Province, College of Information Science and Electronic Engineering, Zhejiang University, Hangzhou 310027, China*

Wei Li − *State Key Laboratory on Integrated Optoelectronics, Institute of Semiconductors, Chinese Academy of Sciences, Beijing 100083, China*

Complete contact information is available at:
https://pubs.acs.org/10.1021/acsphotonics.3c00453

Author Contributions

#J.L.J. and J.H.W. contributed equally to this work. L.L., H.T.L., and J.L.J. conceived the project. J.L.J., J.H.W., C.Y.Z., H.M., Y.L., Y.T.Y., M.L.W., K.H.L., R.Z.L., Z.Q.C., G.Y.L., H.D., T.R.J., W.L., M.L., and J.Y.L. fabricated these devices. J.L.J., M.L.W., and C.L.S. designed passive optical devices. J.L.J., J.H.W., H.M., and B.S.S. performed the device measurements. J.L.J. and J.H.W. proposed and executed the experiments and data analysis. L.L., H.T.L., J.H.W., and J.L.J. analyzed the data and wrote the this paper. L.L., H.T.L., and M.L. oversaw the project. All authors commented on the manuscript.

■ REFERENCES

(1) Koch, U.; Uhl, C.; Hettrich, H.; Fedoryshyn, Y.; Hoessbacher, C.; Heni, W.; Baeuerle, B.; Bitachon, B. I.; Josten, A.; Ayata, M.; Xu, H.; Elder, D. L.; Dalton, L. R.; Mentovich, E.; Bakopoulos, P.; Lischke, S.; Krüger, A.; Zimmermann, L.; Tsiokos, D.; Pleros, N.; Möller, M.; Leuthold, J. A Monolithic Bipolar CMOS Electronic-plasmonic High-speed Transmitter. *Nat. Electron.* **2020**, *3* (6), 338−345.

(2) Winzer, P. J.; Neilson, D. T. From Scaling Disparities to Integrated Parallelism: A Decathlon for a Decade. *J. Light. Technol.* **2017**, *35* (5), 1099−1115.

(3) Alexoudi, T.; Terzenidis, N.; Pitris, S.; Moralis-Pegios, M.; Maniotis, P.; Vagionas, C.; Mitsolidou, C.; Mourgias-Alexandris, G.; Kanellos, G. T.; Miliou, A.; Vyrsokinos, K.; Pleros, N. Optics in Computing: From Photonic Network-on-Chip to Chip-to-Chip Interconnects and Disintegrated Architectures. *J. Light. Technol.* **2019**, *37* (2), 363−379.

(4) Koch, U.; Uhl, C.; Hettrich, H.; Fedoryshyn, Y.; Moor, D.; Baumann, M.; Hoessbacher, C.; Heni, W.; Baeuerle, B.; Bitachon, B. I.; Josten, A.; Ayata, M.; Xu, H.; Elder, D. L.; Dalton, L. R.; Mentovich, E.; Bakopoulos, P.; Lischke, S.; Krüger, A.; Zimmermann, L.; Tsiokos, D.; Pleros, N.; Möller, M.; Leuthold, J. Plasmonics-high-speed Photonics for Co-integration with Electronics. *Jpn. J. Appl.l Phys.* **2021**, *60* (SB), SB0806.

(5) Gramotnev, D. K.; Bozhevolnyi, S. I. Plasmonics beyond the Diffraction Limit. *Nat. Photonics.* **2010**, *4* (2), 83−91.

(6) Melikyan, A.; Kohl, M.; Sommer, M.; Koos, C.; Freude, W.; Leuthold, J. Photonic-to-plasmonic Mode Converter. *Opt. Lett.* **2014**, *39* (12), 3488−3491.

(7) Melikyan, A.; Alloatti, L.; Muslija, A.; Hillerkuss, D.; Schindler, P. C.; Li, J.; Palmer, R.; Korn, D.; Muehlbrandt, S.; Van Thourhout, D.; Chen, B.; Dinu, R.; Sommer, M.; Koos, C.; Kohl, M.; Freude, W.; Leuthold, J. High-speed Plasmonic Phase Modulators. *Nat. Photonics.* **2014**, *8* (3), 229−233.

(8) Haffner, C.; Chelladurai, D.; Fedoryshyn, Y.; Josten, A.; Baeuerle, B.; Heni, W.; Watanabe, T.; Cui, T.; Cheng, B.; Saha, S.; Elder, D. L.; Dalton, L. R.; Boltasseva, A.; Shalaev, V. M.; Kinsey, N.; Leuthold, J. Low-loss Plasmon-assisted Electro-optic Modulator. *Nature.* **2018**, *556* (7702), 483−486.

(9) Ummethala, S.; Harter, T.; Koehnle, K.; Li, Z.; Muehlbrandt, S.; Kutuvantavida, Y.; Kemal, J.; Marin-Palomo, P.; Schaefer, J.; Tessmann, A.; Garlapati, S. K.; Bacher, A.; Hahn, L.; Walther, M.; Zwick, T.; Randel, S.; Freude, W.; Koos, C. THz-to-optical Conversion in Wireless Communications Using an Ultra-broadband Plasmonic Modulator. *Nat. Photonics.* **2019**, *13* (8), 519−524.

(10) Michel, J.; Liu, J.; Kimerling, L. C. High-performance Ge-on-Si Photodetectors. *Nat. Photonics.* **2010**, *4* (8), 527−534.

(11) Ito, H.; Kodama, S.; Muramoto, Y.; Furuta, T.; Nagatsuma, T.; Ishibashi, T. High-speed and High-output InP-InGaAs Unitraveling-carrier Photodiodes. *IEEE J. Quantum Electron.* **2004**, *10* (4), 709−727.

(12) Salamin, Y.; Ma, P.; Baeuerle, B.; Emboras, A.; Fedoryshyn, Y.; Heni, W.; Cheng, B.; Josten, A.; Leuthold, J. 100 GHz Plasmonic Photodetector. *ACS Photonics.* **2018**, *5* (8), 3291−3297.

(13) Soler, M.; Scholtz, A.; Zeto, R.; Armani, A. M. High-performance Infrared Ge-based Plasmonic Photodetector Enhanced by Dual Absorption Mechanism. *APL Photonics* **2020**, *5* (9), 096104.

(14) Zhu, B.; Chen, M.; Zhu, Q.; Zhou, G.; Abdelazim, N. M.; Zhou, W.; Kershaw, S. V.; Rogach, A. L.; Zhao, N.; Tsang, H. K. Integrated Plasmonic Infrared Photodetector Based on Colloidal HgTe Quantum Dots. *Adv. Mater. Technol.* **2019**, *4* (10), 8.

(15) Tong, L.; Huang, X.; Wang, P.; Ye, L.; Peng, M.; An, L.; Sun, Q.; Zhang, Y.; Yang, G.; Li, Z.; Zhong, F.; Wang, F.; Wang, Y.; Motlag, M.; Wu, W.; Cheng, G. J.; Hu, W. Stable Mid-infrared Polarization Imaging based on Quasi-2D Tellurium at Room Temperature. *Nat. Commun.* **2020**, *11* (1), 2308.

(16) Wu, J.; Wei, M.; Mu, J.; Ma, H.; Zhong, C.; Ye, Y.; Sun, C.; Tang, B.; Wang, L.; Li, J.; Xu, X.; Liu, B.; Li, L.; Lin, H. High-Performance Waveguide-Integrated Bi₂O₂Se Photodetector for Si Photonic Integrated Circuits. *ACS Nano* **2021**, *15* (10), 15982−15991.

(17) Ding, Y.; Cheng, Z.; Zhu, X.; Yvind, K.; Dong, J.; Galili, M.; Hu, H.; Mortensen, N. A.; Xiao, S.; Oxenløwe, L. K. Ultra-compact Integrated Graphene Plasmonic Photodetector with Bandwidth above 110 GHz. *Nanophotonics.* **2020**, *9* (2), 317−325.

(18) Ma, P.; Salamin, Y.; Baeuerle, B.; Josten, A.; Heni, W.; Emboras, A.; Leuthold, J. Plasmonically Enhanced Graphene Photodetector Featuring 100 Gbit/s Data Reception, High Responsivity, and Compact Size. *ACS Photonics.* **2019**, *6* (1), 154−161.

(19) Ma, H.; Wu, J.; Wang, Y.; Zhong, C.; Ye, Y.; Wei, M.; Yu, R.; Du, Y.; Tang, B.; Sun, C.; Shi, Y.; Sun, C.; Wang, L.; Zhu, H.; Qiao, X.; Li, L.; Lin, H. Enhanced Light-Tellurium Interaction through Evanescent Wave Coupling for High Speed Mid-Infrared Photodetection. *Adv. Opt. Mater.* **2022**, *10* (23), 2201443.

(20) Wang, X.; Cheng, Z.; Xu, K.; Tsang, H. K.; Xu, J.-B. High-responsivity Graphene/silicon-heterostructure Waveguide Photodetectors. *Nat. Photonics.* **2013**, *7* (11), 888−891.

(21) Freitag, M.; Low, T.; Xia, F.; Avouris, P. Photoconductivity of Biased Graphene. *Nat. Photonics.* **2013**, 7 (1), 53−59.

(22) Youngblood, N.; Chen, C.; Koester, S. J.; Li, M. Waveguide-integrated Black Phosphorus Photodetector with High Responsivity and Low Dark Current. *Nat. Photonics.* **2015**, 9 (4), 247−252.

(23) Ye, L.; Li, H.; Chen, Z.; Xu, J. Near-Infrared Photodetector Based on MoS_2/Black Phosphorus Heterojunction. *ACS Photonics.* **2016**, 3 (4), 692−699.

(24) Wood, J. D.; Wells, S. A.; Jariwala, D.; Chen, K.-S.; Cho, E.; Sangwan, V. K.; Liu, X.; Lauhon, L. J.; Marks, T. J.; Hersam, M. C. Effective Passivation of Exfoliated Black Phosphorus Transistors against Ambient Degradation. *Nano Lett.* **2014**, 14 (12), 6964−6970.

(25) Liang, Q.; Wang, Q.; Zhang, Q.; Wei, J.; Lim, S. X.; Zhu, R.; Hu, J.; Wei, W.; Lee, C.; Sow, C.; Zhang, W.; Wee, A. T. S. High-Performance, Room Temperature, Ultra-Broadband Photodetectors Based on Air-Stable $PdSe_2$. *Adv. Mater.* **2019**, 31 (24), No. e1807609.

(26) Hoffman, A. N.; Gu, Y.; Liang, L.; Fowlkes, J. D.; Xiao, K.; Rack, P. D. Exploring the Air Stability of $PdSe_2$ via Electrical Transport Measurements and Defect Calculations. *npj 2D Mater. Appl.* **2019**, 3 (1), 50.

(27) Luo, L. B.; Wang, D.; Xie, C.; Hu, J. G.; Zhao, X. Y.; Liang, F. X. $PdSe_2$ Multilayer on Germanium Nanocones Array with Light Trapping Effect for Sensitive Infrared Photodetector and Image Sensing Application. *Adv. Funct. Mater.* **2019**, 29 (22), 1900849−1900857.

(28) Cheng, P. K.; Tang, C. Y.; Ahmed, S.; Qiao, J.; Zeng, L.-H.; Tsang, Y. H. Utilization of Group 10 2D TMDs-$PdSe_2$ as a Nonlinear Optical Material for Obtaining Switchable Laser Pulse Generation Modes. *Nanotechnology.* **2021**, 32 (5), 055201−055211.

(29) Sun, J.; Shi, H.; Siegrist, T.; Singh, D. J. Electronic, Transport, and Optical Properties of Bulk and Mono-layer $PdSe_2$. *Appl Phys. Lett.* **2015**, 107, 153902.

(30) Wang, Y.; Zhou, Y.; Zhang, Z.; Xiao, S.; Xu, J.-b.; Tsang, H. K. 40 GHz Waveguide-integrated Two-dimensional Palladium Diselenide Photodetectors. *Appl. Phys. Lett.* **2022**, 120 (23), 231102−231109.

(31) Wu, J.; Ma, H.; Zhong, C.; Wei, M.; Sun, C.; Ye, Y.; Xu, Y.; Tang, B.; Luo, Y.; Sun, B.; Jian, J.; Dai, H.; Lin, H.; Li, L. Waveguide-Integrated $PdSe_2$ Photodetector over a Broad Infrared Wavelength Range. *Nano Lett.* **2022**, 22 (16), 6816−6824.

(32) Ma, Z.; Kikunaga, K.; Wang, H.; Sun, S.; Amin, R.; Maiti, R.; Tahersima, M. H.; Dalir, H.; Miscuglio, M.; Sorger, V. J. Compact Graphene Plasmonic Slot Photodetector on Silicon-on-Insulator with High Responsivity. *ACS Photonics.* **2020**, 7 (4), 932−940.

(33) Long, M.; Wang, P.; Fang, H.; Hu, W. Progress, Challenges, and Opportunities for 2D Material Based Photodetectors. *Adv. Funct. Mater.* **2019**, 29 (19), 1803807−1803836.

(34) Gao, Y.; Tao, L.; Tsang, H. K.; Shu, C. Graphene-on-silicon Nitride Waveguide Photodetector with Interdigital Contacts. *Appl. Phys. Lett.* **2018**, 112 (21), 211107−211113.

(35) Blauth, M.; Vest, G.; Rosemary, S. L.; Prechtl, M.; Hartwig, O.; Jürgensen, M.; Kaniber, M.; Stier, A. V.; Finley, J. J. Ultracompact Photodetection in Atomically Thin $MoSe_2$. *ACS Photonics.* **2019**, 6 (8), 1902−1909.

(36) Wang, Y.; Yu, Z.; Zhang, Z.; Sun, B.; Tong, Y.; Xu, J.-B.; Sun, X.; Tsang, H. K. Bound-States-in-Continuum Hybrid Integration of 2D Platinum Diselenide on Silicon Nitride for High-Speed Photodetectors. *ACS Photonics.* **2020**, 7 (10), 2643−2649.

(37) Tian, R.; Gan, X.; Li, C.; Chen, X.; Hu, S.; Gu, L.; Van Thourhout, D.; Castellanos-Gomez, A.; Sun, Z.; Zhao, J. Chip-integrated van der Waals PN Heterojunction Photodetector with Low Dark Current and High Responsivity. *Light Sci. Appl.* **2022**, 11 (1), 101.

(38) Li, H.; Anugrah, Y.; Koester, S. J.; Li, M. Optical Absorption in Graphene Integrated on Silicon Waveguides. *Appl. Phys. Lett.* **2012**, 101 (11), 111110−111116.

(39) Chen, T.; Bobbert, P. A.; van der Wiel, W. G. 1/f Noise and Machine Intelligence in a Nonlinear Dopant Atom Network. *Small. Sci.* **2021**, 1 (3), 2000014.

(40) Balandin, A. A. Low-frequency 1/f Noise in Graphene Devices. *Nat. Nanotechnol.* **2013**, 8 (8), 549−555.

(41) Dereniak, E. L. *Infrared Detectors and Systems*; A Wiley-Interscience Publication, 1996.

(42) Pospischil, A.; Humer, M.; Furchi, M. M.; Bachmann, D.; Guider, R.; Fromherz, T.; Mueller, T. CMOS-compatible Graphene Photodetector Covering all Optical Communication Bands. *Nat. Photonics.* **2013**, 7 (11), 892−896.

(43) Wang, Y.; Yu, Z.; Tong, Y.; Sun, B.; Zhang, Z.; Xu, J.-B.; Sun, X.; Tsang, H. K. High-speed Infrared Two-dimensional Platinum Diselenide Photodetectors. *Appl. Phys. Lett.* **2020**, 116 (21), 6.

(44) Liu, C.; Guo, J.; Yu, L.; Xiang, Y.; Xiang, H.; Li, J.; Dai, D. High-Speed and High-Responsivity Silicon/Black-Phosphorus Hybrid Plasmonic Waveguide Avalanche Photodetector. *ACS Photonics.* **2022**, 9 (5), 1764−1774.

(45) Oyedele, A. D.; Yang, S.; Liang, L.; Puretzky, A. A.; Wang, K.; Zhang, J.; Yu, P.; Pudasaini, P. R.; Ghosh, A. W.; Liu, Z.; Rouleau, C. M.; Sumpter, B. G.; Chisholm, M. F.; Zhou, W.; Rack, P. D.; Geohegan, D. B.; Xiao, K. $PdSe_2$: Pentagonal Two-Dimensional Layers with High Air Stability for Electronics. *J. Am. Chem. Soc.* **2017**, 139 (40), 14090−14097.

(46) Xia, F.; Mueller, T.; Lin, Y. M.; Valdes-Garcia, A.; Avouris, P. Ultrafast Graphene Photodetector. *Nat. Nanotechnol.* **2009**, 4 (12), 839−843.

(47) Guo, J.; Li, J.; Liu, C.; Yin, Y.; Wang, W.; Ni, Z.; Fu, Z.; Yu, H.; Xu, Y.; Shi, Y.; Ma, Y.; Gao, S.; Tong, L.; Dai, D. High-performance Silicon-graphene Hybrid Plasmonic Waveguide Photodetectors beyond 1.55 μm. *Light Sci. Appl.* **2020**, 9, 29.